JPhys Materials

PAPER • OPEN ACCESS

Mechanical properties of colloidal crystals at fluid interfaces

To cite this article: Ivo Buttinoni and Roel P A Dullens 2021 *J. Phys. Mater.* **4** 025001

IOP Publishing J. Phys. Mater. 4 (2021) 025001 https://doi.org/10.1088/2515-7639/abd019

Journal of Physics: Materials

OPEN ACCESS

RECEIVED
13 October 2020

REVISED
26 November 2020

ACCEPTED FOR PUBLICATION
2 December 2020

PUBLISHED
12 January 2021

PAPER

Mechanical properties of colloidal crystals at fluid interfaces

Ivo Buttinoni[1,2] and Roel P A Dullens[2]

[1] Department of Physics, Institute of Experimental Colloidal Physics, Heinrich-Heine University, Universitätsstr. 1, Düsseldorf 40225, Germany

[2] Department of Chemistry, Physical and Theoretical Chemistry Laboratory, University of Oxford, South Parks Road, Oxford OX1 3QZ, United Kingdom

E-mail: ivo.buttinoni@hhu.de

Keywords: colloids, colloidal crystals, optical tweezers, fluid interfaces

Abstract

We characterise the local mechanical properties of two-dimensional colloidal crystals with hexagonal symmetry assembled at the flat interface between oil and water. Our experiments elucidate the conditions under which the material behaves isotropically, as opposed to those where the microstructure plays a major role. Brownian fluctuations are used to extract the stiffness of the lattice under the continuum approximation, whereas at larger displacements, obtained by optically driving one particle through the structure, the mechanical resistance of the lattice depends on both the area fraction and the direction of the applied force. Remarkably, the minimum resistance does not necessarily correspond to a probe being driven between neighbours, i.e. at 30° with respect to the crystal axes.

1. Introduction

Colloidal crystals are one of the most compelling examples of assemblies of microscopic particles used as model playgrounds for atomic materials [1]. In addition to the observable size of the building units (i.e. the colloidal particles), lattices made of microparticles suspended in a fluid easily deform (or relax) under thermal fluctuations, weak external fields and shear flows [2]. This soft response has prompted groundbreaking experiments that shed light on many fundamental problems including 3D and 2D melting [3–5], grain boundaries [6–10] and defects [11, 12] dynamics, vibrational modes [13–15], and wave propagation [16, 17].

The mechanical characterisation of colloidal crystals is often carried out at a coarse-grained level using commercial or custom-made rheometers [18–20]. These experiments rely on bulk oscillatory or steady shear flows and, therefore, local information about the microstructure of the lattice is lost. A closer focus on local structural rearrangements can be provided using miniaturised probes, i.e. microscopic objects that are dragged through the colloidal crystal by means of external magnetic [21–23] or optical fields [24], a research field known as active microrheology [25]. In particular, laser-based microrheology allows to optically trap a microprobe, drive it at constant velocity and, simultaneously, measure the force exerted on it by the surrounding structure [24, 26, 27]. Nonetheless, the driven probes can be still regarded as 'intruders'; they are typically larger than the particles of the crystal due to difficulties in tweezing single colloids confined in nearly close-packed lattices. Two-dimensional crystals of strongly repulsive microparticles are a remarkable exception since the lattice constant is typically much larger than the diameter of the particles. They can be fabricated using charged particles in low-polar solvents [28], superparamagnetic colloids [5, 14, 15] or by spreading sulphate latex particles at flat water-oil interfaces [29, 30]. For sparse lattices, it was shown that optical tweezing can be employed to manipulate selected particles of the crystal and impose 'internal stresses' (note that the driving force is nonetheless external) [28]. The latter reference elucidated the mechanisms of stress relaxation down to the unit cell level, but did not measure the forces required to internally deform the colloidal lattices. While a 'passive' characterisation based on spatial correlations in equilibrium revealed that two-dimensional crystals behave as harmonic lattices upon small deformations [14], a link to the 'active'

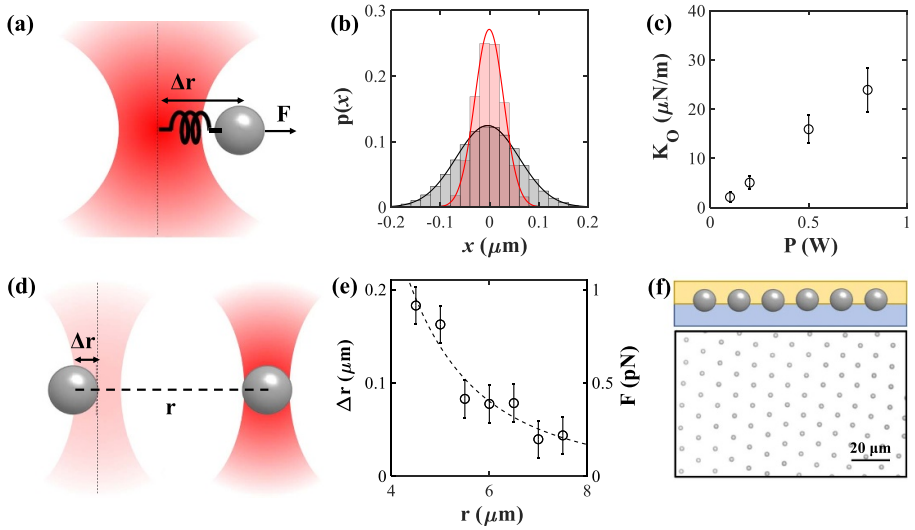

Figure 1. (a) Sketch of a spherical particle confined in an optical potential. The optical trap behaves as a spring and external forces are measured by looking at the displacement Δr. (b) Spatial probability distribution of colloidal particles inside two traps of stiffness $K_O^{(1)} = 5\ \mu\mathrm{N\,m^{-1}}$ (black) and $K_O^{(2)} = 26\ \mu\mathrm{N\,m^{-1}}$ (red). The solid lines are Gaussian fits. (c) Linear dependence of K_O as a function of the nominal power P of the laser. (d) Sketch of the experimental method used to extract the force F between two colloids at relative distance r: the force is proportional to the displacement Δr of the weakly trapped particle. (e) Δr and F as a function of r. The dashed line corresponds to a power law fit according to $y \sim x^{-n}$ (R-squared = 85%), where n is found to be equal to 3.65. (f) Sketch of colloidal particles adsorbed at the water–oil interface and bright-field microscopy image of colloidal crystal ($L/R = 9.5$).

experiments, where probe particles are driven by an external force and therefore impose larger strains, is still lacking.

This paper is motivated by the following two main questions: when does the harmonic approximation of a colloidal lattice break down? And if the crystals behave no longer as isotropic solids, how does the microstructure affect the ability to displace particles along different directions? To answer these questions we consider two-dimensional colloidal crystals with soft interactions and look at fluctuating test particles as well as particles driven through the lattice by means of an optical tweezer. We find that the response to small strain amplitudes, whether 'passive' or 'active', obeys the continuum (harmonic) approximation, whereas larger deformations are sensitive to the microstructure of the material. In the second regime, the mechanical resistance of the monolayers to an externally driven particle changes with the direction of the applied deformation relative to the crystal orientation. Remarkably, the direction of least resistance does not always coincide to the case in which the probe is driven exactly between nearest neighbours. The remainder of the manuscript is structured as follows. We first describe the experimental methods (section 2), in particular, the preparation of colloidal crystals at liquid interfaces and the measurement of forces using optical tweezers. In section 3, the stiffness of the lattices is extracted from the thermal fluctuations of probe particles. We then measure the forces required to drag a particle over one unit cell as a function of the lattice constant and the direction of the driving force (section 4). We finally summarise and suggest some future research directions.

2. Experimental methods

The oil–water interface is prepared as follows; first we glue a sharp-edged metallic ring onto a #0 cover slip and fill it with 2 μl of deionised water. Hexadecane is then poured on top and contained by a larger ring made of Teflon. The resulting flat interface is strongly pinned to the inner edge of the metallic ring and any evaporation is prevented by the low volatility of the oil phase. Sulfate polystyrene particles (radius, $R = 1.4\ \mu$m, Microparticles GmbH) are added to the interface by means of a 1:1 water–isopropyl alcohol spreading solution. The colloids are adsorbed at the interface with energies larger than 1000 $k_B T$ ($k_B T$ is the thermal energy) and $\approx 120°$ contact angles [31]. Due to the large adsorption energies, the particles only undergo two-dimensional displacements in the xy-plane of the interface with drag forces that are determined by an effective viscosity, $\eta_W < \eta < \eta_O$, where η_W and η_O are the viscosity of water and hexadecane, respectively. For simplicity, we assume $\eta = 2$ mPa·s [31]. The colloidal particles are imaged in transmission at 10 frames per second using a 40× objective and a Ximea MQ013MG-E2 CMOS camera; two-dimensional Brownian motion is observed in the dilute regime in the absence of external fields [31].

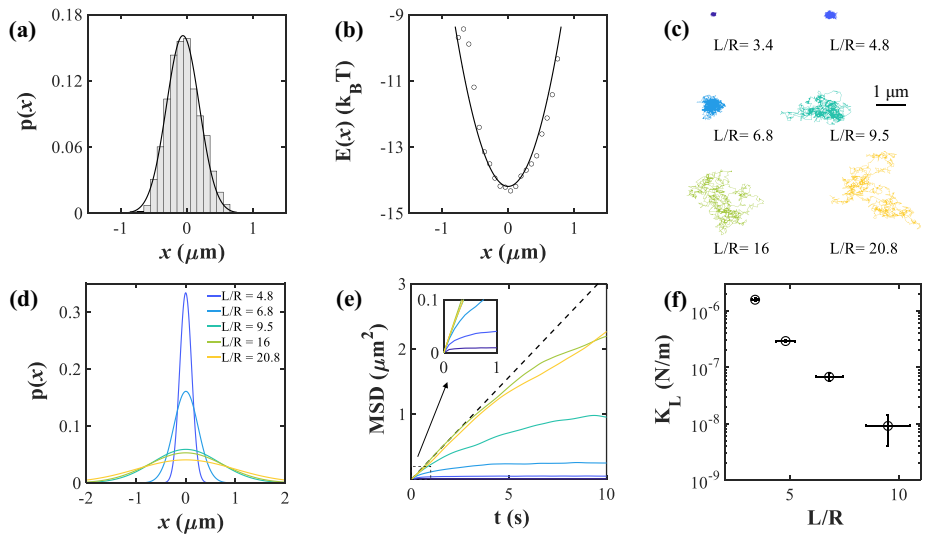

Figure 2. (a) Histogram of the x-coordinates distribution for a Brownian particle belonging to colloidal crystal ($L/R = 6.8$) assembled at the water–oil interface. The solid line corresponds to the Gaussian fits. (b) Potential energy calculated from (a) as described in the main text. Each dot correspond to a bin of $p(x)$ and the solid line is a parabolic fitting curve (R-squared = 96%). (c) Trajectories of Brownian particles jiggling about their lattice sites, in monolayers with different packing fraction. (d) Gaussian fits of the spatial probability distributions and (e) mean squared displacements as a function of time. The colours are against L/R. In all experiments the acquisition time is 100 s and any drift is removed before data analysis.

The optical tweezing setup consists of an infrared laser (Coherent Compass 1064-4000 M, wavelength, $\lambda = 1064$ nm) that is steered by two acousto-optic deflectors (AOD, Opto-Electronic DTSXY-250-1064) and focused on the sample plane by a 50× trapping objective [32, 33]. The optical trap behaves as a confining spring (figure 1(a)) such that the displacement of a trapped particle with respect to the trap's centre can be used to measure the magnitude of an external force acting on it [34]. The stiffness K_O, i.e. the spring constant of the optical potential, is calibrated by measuring the variance $\langle x^2 \rangle$ of the Gaussian spatial probability distribution $p(x)$ along the x-axis of a trapped Brownian particle [34]: the weaker the trap, the broader the distribution. Two examples are shown in figure 1(b). K_O increases linearly with the nominal laser power P (figure 1(c)) up to ≈1 W. At the liquid interface, we carefully checked that the laser traps does not induce any heating or deformation of the meniscus around the adsorbed colloids; if these effects were relevant, we would in fact observe power-dependent convective flows and capillary forces [35].

The pair potential U is repulsive and long-ranged due the inhomogeneous distribution of ions between the two liquids and the presence of residual charges near the oil-wetted particle surface [1]. Theoretical [36–38] and experimental [39–41] works showed that the interaction energy scales as r^{-3}, where r is the relative centre-to-centre distance. We also measure these interactions by confining two particles in traps of different stiffnesses (a 'weak trap' and a 'strong trap', with stiffnesses $K_O^{(W)}$ and $K_O^{(S)}$, respectively) and decreasing step-wise their relative distance r . The strongly-trapped particle remains fixed, whereas the colloid in the weak trap is displaced by Δr from the centre of its trap as the relative distance r decreases (see sketch in figure 1(d)). Figure 1(e) shows that the force, $F = \mathrm{d}U/\mathrm{d}r = K_O^{(W)}\Delta r$, indeed approximately scales as r^{-4}. The long-ranged potential leads to the formation of polycrystalline monolayers with hexagonal symmetry (figure 1(f), L is the lattice spacing) down to very small packing fractions, whereas deep quenching is achieved by increasing the particle concentration of the spreading solution [21]. This allows us to study the mechanical properties of colloidal crystals over a large range of lattice constants. The packing of the lattice can alternatively be expressed in terms of the area fraction, $\phi = \left(2\pi R^2\right) / \left(\sqrt{3}L^2\right)$, or the 2D number density, $\rho = 2/\left(\sqrt{3}L^2\right)$.

3. Stiffness of the lattices

Colloidal particles can be driven through a crystal provided that K_O is larger than the stiffness of the lattice, K_L. We estimate K_L by looking at the diffusive motion of probe particles in the crystal, under no optical fields. Due to the confinement in the hexagonal cage and the small displacements arising from Brownian motion, the spatial fluctuations are understood as a diffusive process inside a two-dimensional parabolic potential, whose width is given by K_L. Figure 2(a) shows the Gaussian spatial probability distribution along the x-axis for a Brownian particle belonging to a crystalline monolayer, after subtracting any small drift due

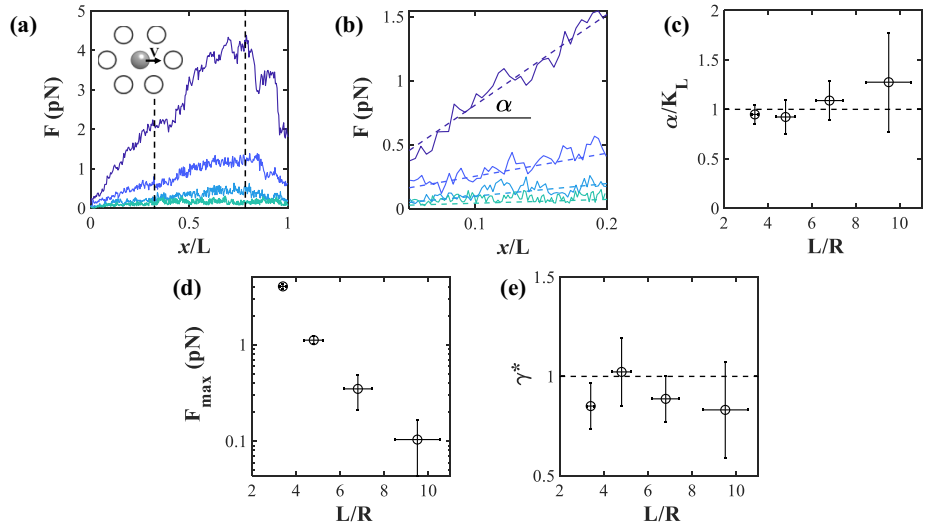

Figure 3. (a) Force *vs.* normalised travelled distance measured while driving a particle at $V = 0.2\ \mu\mathrm{m\,s^{-1}}$ along a symmetry axis of the crystalline interfaces (inset). The colours correspond to different values of L/R, from 3.4 (dark blue) to 9.5 (light blue), and match the data shown in figures 2(c) and (e). The vertical dashed lines approximately mark the three regimes discussed in the main text. (b) Close-up of panel (a) for small values of x/L. The dashed lines are linear fits whose slope is denoted as α. (c) Ratio between α and K_L (taken from figure 2(f)); Brownian fluctuations and small-displacement optical tweezing experiments measure the same lattice stiffness. (d) Maximum force as a function of L/R, measured before the driven particle enters a new unit cell. (e) Critical strain γ^* evaluated at $F = F_\mathrm{max}$ and plotted against L/R. The horizontal dashed lines in panels (c) and (e) are drawn to guide the eye.

to convective flows at the interface [31, 42]. The quadratic behaviour of the corresponding potential energy distribution $E(x)$, obtained using the Boltzmann relation $p(x) \propto \exp(-E(x)/k_\mathrm{B}T)$, is verified in figure 2(b) up to a constant.

This simple yet powerful method is applied to six crystalline monolayers of increasing area fraction, from $L/R = 3.4$ ($\phi = 31\%$, $\rho = 0.051\ \mu\mathrm{m}^{-2}$) to $L/R = 20.8$ ($\phi = 1\%$, $\rho = 0.0014\ \mu\mathrm{m}^{-2}$), averaging over ≈10 particles each. Examples of particle trajectories are illustrated in figure 2(c). The corresponding Gaussian fitting curves of $p(x)$ become broader as the lattice constant increases (figure 2(d)). Broader distributions could also indicate that the particle is not effectively confined by the lattice within our experimental timescale, since $\langle x^2 \rangle$ of freely diffusing particles grows linearly over time. To check that $\langle x^2 \rangle$ uniquely determines K_L, we further calculate the mean squared displacement (MSD) of the colloids as a function of time (figure 2(e)), which also undergoes a linear increase in the case of freely-diffusing particles, but flattens in isotropic confinements. While we are able to observe the plateau up to $L/R = 9.5$, sparser lattices do not provide enough confinement within our experimental timescale (≈100 s). For $L/R = 16$ and $L/R = 20.8$, we even recover a freely-diffusive 2D Brownian motion with diffusion coefficient $D = (k_\mathrm{B}T)/(6\pi\eta R)$ (see dashed line in figure 2(e)). The following results are therefore limited to crystals whose lattice spacing is smaller than $10R$. Figure 2(f) shows the stiffness of the loosely-packed crystals at the liquid interface, i.e. $K_\mathrm{L} = 2E(x)/x^2$, which ranges from 1.5 $\mu\mathrm{N\,m^{-1}}$ down to less than 10 $\mathrm{nN\,m^{-1}}$.

We emphasise that, while former works have determined the spring constant of two-dimensional crystals made of paramagnetic particles using spatial correlations [14], the data in figure 2(f) are simply based on Brownian fluctuations of probe particles. To the best of our knowledge, they constitute the first measurement of the stiffness of colloid-laden interfaces where the particles predominately interact via electric forces and will therefore aid future works aimed at characterising the rheological response of this widespread two-dimensional colloidal system [43]. The values of K_L are also smaller than the spring constant used in the following ($K_\mathrm{O} = 2.12\ \mu\mathrm{N\,m^{-1}}$), thus making it possible to optically drive probe particles through the two-dimensional lattice.

4. Measurement of forces

By trapping a probe particle of the crystal and looking at its position with respect to the centre of the trap (figure 1(a)), we measure the force it takes to move it over one lattice constant, L, along one of the six crystal axes, as sketched in the inset of figure 3(a). The optical driving takes place at relative velocity $V = 0.2\ \mu\mathrm{m\,s^{-1}}$ (experimentally we hold the particle and move the stage), which is small enough so that the viscous drag force, $F_D = 6\pi\eta RV$, is one to two orders of magnitude smaller than the forces exerted by the lattice. We also

only consider defects-free regions of the crystal. The curves in figure 3(a) illustrates the measured force, F, as a function of the normalised travelled distance, x/L, for monolayers of different area fraction. In dense crystals (e.g. dark blue data), three regimes can be discerned: an initial linear increase, which is followed by a second growth until F reaches a maximum and suddenly drops. The linear increase corresponds to the Hookean approximation of the crystals, according to which there is a linear relation between stresses and strains. The slope α of the linear fits (figure 3(b)) is the elastic modulus, i.e. the stiffness of the colloid laden interfaces. Figure 3(c) reveals a remarkable agreement, for all packing fractions, with the stiffness K_{L} extracted from Brownian fluctuations (figure 2(f)), which, nonetheless, remains a less invasive method to probe the material. In the second regime, the probe becomes sensitive to the heterogeneity of the lattice and, as such, to its structural response when local strain is applied; a simple relation between F and x/L no longer exists. When the local deformation becomes too large, F plateaus to the value F_{max} and quickly decreases soon after. F_{max} is smaller for larger values of L/R (figure 3(d)), confirming that the driven probe particle encounters less resistance as the crystals become more loosely-packed. Local yielding occurs when $F = F_{\mathrm{max}}$, at $(x/L)^*$; the monolayers no longer sustain the applied strain and undergo plastic rearrangements such that the driven probes hop into a different unit cells. Figure 3(e) shows that the critical strain, $\gamma^* = 2\,(x/L)^*/\sqrt{3}$ (the factor $\sqrt{3}/2$ takes into account the hexagonal symmetry of the unit cell) does not depend on the packing density of the crystal and is approximately equal to 1, in agreement with previous observations under shear flow [21].

We repeated the experiments along other driving directions, i.e. at angles between $0 < \theta < \pi/6$, where θ is the angle between the orientation of V and the nearest crystal axis, and define the monolayer's resistance as the maximum force measured between $x/L = 0$ and $x/L = 1$. In figure 4(a), we compare the limiting cases of $\theta = 0$ (black data) and $\theta = \pi/6$ (red data). The overlap of the first linear increase of the two curves is a strong evidence that the microstructure of the lattice can be disregarded for small displacements; the crystals behaves as an isotropic two-dimensional solid [44]. Instead, larger displacements reveal significant differences. If $\theta = \pi/6$ (red curve), the maximum force occurs at larger distances, $x/L \approx 1$ (compare the dashed vertical lines in figure 4(a)), and is determined by the particle that belongs to the next unit cell. This phenomenology is also described by the particle trajectories in figures 4(b) and (c) (the colour codes are used to denote the time, as explained in the caption). Displacements along the symmetry axis (figure 4(b)) set into motion only the corresponding chain of particles until the applied stress is relaxed via rearrangement loops, which have been also observed in reference [28] and ascribed to transiently generated circular grain boundaries. In contrast, a probe particle that is driven between two nearest neighbours (figure 4(c)) comes across two main barriers: a first barrier when the neighbours are displaced sideways and stronger one that occurs as soon as the probe 'feels' the next particle sitting along its linear path.

Figure 4(d) shows the maximum force measured before the probe leaves its unit cell ($x/L < 1$) as a function of the driving angle for monolayers with $L/R = 3.4$. While the isotropic response at small x/L is consistently recovered for all data sets (see Inset), the behaviour of F_{max} is remarkably non-monotonic. The minimum is not observed in experiments in which the probe particles are dragged exactly between two neighbours ($\theta = \pi/6$), but rather when we introduce a small mismatch, i.e. at $\theta \approx \pi/9$. A similar trend is observed if, instead of using F_{max} as reference for the resistance of the lattice, we plot the work W needed to drag the probe over a distance $L/2$, L and $2L$ through the crystalline monolayers (figure 4(e)). Here, W is the sum of the integral of the force-displacement curves and the viscous contribution:

$$W = \int_0^L F\mathrm{d}x + 6\pi\eta VL. \tag{1}$$

Beyond the linear regime ($x/L > 1/2$), the work exhibits a minimum at $\theta \approx \pi/9$. This result suggest that the easiest way to deform a crystalline lattice is not trivial and can include directions that are not defined *a priori* by the microstructure. In figure 4(f), we plot F_{max} as a function of θ for three different lattice spacings. Since the magnitude of F_{max} depends on the density of the crystal (see, for instance, figure 3(d)), for each L/R we normalised F_{max} using its maximum value, F^*_{max}. For all values of L/R, the highest resistance of the lattice corresponds to the probe particle being driven along the crystal axis ($F^*_{\mathrm{max}} = F_{\mathrm{max}}(\theta = 0)$). This result is consistent with the inset of figure 4(a) but not trivial *a priori* due to collective particle rearrangements (figure 4(b)). Instead, the lowest resistance, i.e. the minimum of the curves in figure 4(f), varies depending on L/R, showing that the dynamic response of the structure is a complex process involving many-particle rearrangements.

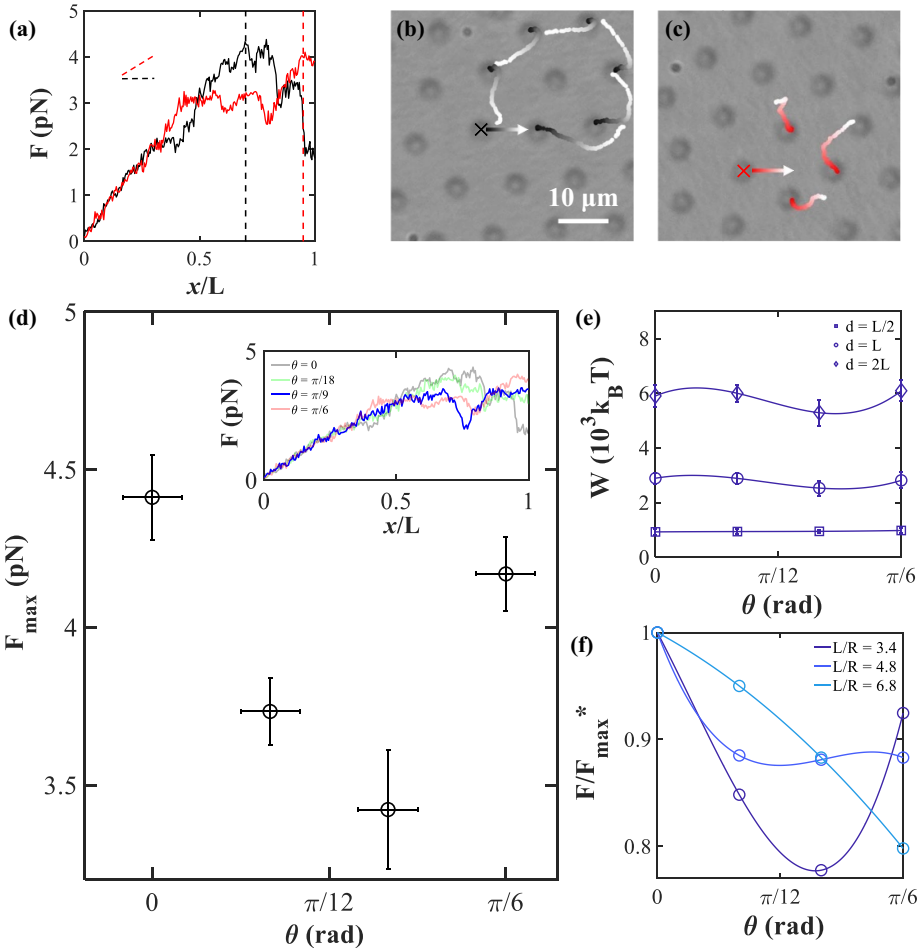

Figure 4. (a) Force *vs.* normalised travelled distance measured while driving a particle at $V = 0.2\ \mu\mathrm{m\,s^{-1}}$ along a crystal axis (black) and at an angle $\theta = \pi/6$ (red), as illustrated in the inset. The vertical dashed lines mark the positions at which the maximum force is measured. (b) and (c) Trajectories of particles undergoing displacements greater than $2R$, for (b) $\theta = 0$ and (c) $\theta = \pi/6$. The arrows and the crosses mark the motion and the initial positions of the driven probes, respectively. The colours highlight the time, from $t = 0$ (black/red) to $t = L/V$ (white). The images correspond to $t = 0$ s. (d) Maximum force plotted as a function of the direction of driving θ ($L/R = 3.4$), within a unit cell ($x/L < 1$). The error bars are obtained from an average of $\approx$10 particle. The inset shows four F–x/L curves and highlights the one for which the minimum value of F_{max} is measured. (e) Work needed to displace the probe particle by a distance $L/2$ (squares), L (circles) and $2L$ (diamonds). (f) Normalised F_{max} against θ, for monolayers of different area fraction. F^{*}_{max} is the maximum value of F_{max} for a given L/R; it happens to occur at $\theta = 0$ for all L/R. In (e) and (f), the lines are spline interpolations used to improve clarity.

5. Conclusions

We studied the mechanical properties of hexagonal colloidal crystals confined at flat water-oil interfaces. The particles interact via long-ranged repulsive potentials, thus making it possible to study sparse crystalline monolayers with tunable lattice constant. We characterised the mechanical response to the motion of individual probe particles which are locally displaced by means of optical traps. Our measurements support two main conclusions. Firstly, for displacements that are much smaller than the lattice constant, the crystalline monolayers can be approximated by an elastic medium whose stiffness does not depend on the orientation of the driving force relative to the crystal axes (continuum limit). We found excellent agreement with stiffness values calculated by looking at the Brownian fluctuations of the particles, i.e. 'active' and 'passive' mechanical tests are consistent. Secondly, for displacements that are of the order of the lattice constant, the microstructure plays a leading role in determining the force and work needed to drive a particle over one unit cell. The largest mechanical resistance is found when the driving direction corresponds to one of the crystal axes, whereas the smallest lattice forces are reported when we introduce a misorientation angle between the external force and the closest crystal axis. Importantly, this angle depends on the packing of the lattice and does not always coincide to the probe particle being driven exactly between two nearest neighbours.

Our results pave the way to locally measure the mechanical properties of more complex colloidal phases including polycrystalline and glassy monolayers. For example, how do local defects and grain boundaries

affect the internal forces? Our characterisation will also shed light on the physics of active crystals [42, 45], i.e. lattices where particles undergo self-propulsion rather than being dragged by external forces. Can self-propulsion be viewed as an external force without fixed orientation?

Acknowledgments

We thank Joshua Abbott, Miranda Bell-Davies and Arran Curran for helping with the experimental setup. We are also grateful to Dirk Aarts and Kilian Dietrich for useful discussions. IB acknowledges support from the European Commission with a Marie Sklodowska-Curie Individual Fellowship (Grant No. 747029).

ORCID iDs

Ivo Buttinoni https://orcid.org/0000-0002-0067-0712
Roel P A Dullens https://orcid.org/0000-0003-1751-0958

References

[1] Manoharan V N 2015 Colloidal matter: packing, geometry and entropy *Science* **349** 1253751
[2] Pieranski P 1983 Colloidal crystals *Contemp. Phys.* **24** 25–73
[3] Wang Z, Wang F, Peng Y, Zheng Z and Han Y 2012 Imaging the homogeneous nucleation during the melting of superheated colloidal crystals *Science* **338** 87–90
[4] Thorneywork A L, Abbott J L, Aarts D G A L and Dullens R P A 2017 Two-dimensional melting of colloidal hard spheres *Phys. Rev. Lett.* **118** 158001
[5] Zahn K and Maret G 2000 Dynamic criteria for melting in two dimensions *Phys. Rev. Lett.* **85** 3656
[6] Skinner T O E, Aarts D G A L and Dullens R P A 2010 Grain-boundary fluctuations in two-dimensional colloidal crystals *Phys. Rev. Lett.* **105** 168301
[7] Alsayed A M, Islam M F, Zhang J, Collings P J and Yodh A G 2005 Premelting at defects within bulk colloidal crystals *Science* **309** 1207–10
[8] Lavergne Fçois A, Aarts D G A L and Dullens R P A 2017 Anomalous grain growth in a polycrystalline monolayer of colloidal hard spheres *Phys. Rev.* **7** 041064
[9] Lavergne Fçois A, Curran A, Aarts D G A L and Dullens R P A 2018 Dislocation-controlled formation and kinetics of grain boundary loops in two-dimensional crystals *Proc. Natl. Acad. Sci.* **115** 6922–7
[10] Liao M, Xiao X, Chui S T and Han Y 2018 Grain-boundary roughening in colloidal crystals *Phys. Rev.* X **8** 021045
[11] Schall P, Cohen I, Weitz D A and Spaepen F 2004 Visualization of dislocation dynamics in colloidal crystals *Science* **305** 1944–8
[12] Pertsinidis A and Ling X S 2001 Diffusion of point defects in two-dimensional colloidal crystals *Nature* **413** 147–50
[13] Baumgartl Jorg, Dietrich J, Dobnikar J, Bechinger C and von Grünberg H H 2008 Phonon dispersion curves of two-dimensional colloidal crystals: the wavelength-dependence of friction *Soft Matter* **4** 2199–206
[14] Keim P, Maret G, Herz U and von Grünberg H H 2004 Harmonic lattice behavior of two-dimensional colloidal crystals *Phys. Rev. Lett.* **92** 215504
[15] Gratale M D, Yunker P J, Chen K, Still T, Aptowicz K B and Yodh A G 2013 Phonons in two-dimensional colloidal crystals with bond-strength disorder *Phys. Rev.* E **87** 052301
[16] van Doorn J M, Higler R, Wegh R, Fokkink R, Zaccone A, Sprakel J and van der Gucht J 2020 Propagation and attenuation of mechanical signals in ultrasoft 2d solids *Sci. Adv.* **6** eaba6601
[17] Cheng W, Wang J, Jonas U, Fytas G and Stefanou N 2006 Observation and tuning of hypersonic bandgaps in colloidal crystals *Nat. Mater.* **5** 830–6
[18] Haw M D, Poon W C K and Pusey P N 1998 Direct observation of oscillatory-shear-induced order in colloidal suspensions *Phys. Rev.* E **57** 6859
[19] Panine P, Narayanan T, Vermant J and Mewis J 2002 Structure and rheology during shear-induced crystallization of a latex suspension *Phys. Rev.* E **66** 022401
[20] Cohen I, Davidovitch B, Schofield A B, Brenner M P and Weitz D A 2006 Slip, yield and bands in colloidal crystals under oscillatory shear *Phys. Rev. Lett.* **97** 215502
[21] Buttinoni I, Steinacher M, Spanke H T, Pokki J, Bahmann S, Nelson B, Foffi G and Isa L 2017 Colloidal polycrystalline monolayers under oscillatory shear *Phys. Rev.* E **95** 012610
[22] Choi S Q, Jang S G, Pascall A J, Dimitriou M D, Kang T, Hawker C J and Squires T M 2011 Synthesis of multifunctional micrometer-sized particles with magnetic, amphiphilic and anisotropic properties *Adv. Mater.* **23** 2348–52
[23] Keim N C and Arratia P E 2015 Role of disorder in finite-amplitude shear of a 2D jammed material *Soft Matter* **11** 1539–46
[24] Dullens R P A and Bechinger C 2011 Shear thinning and local melting of colloidal crystals *Phys. Rev. Lett.* **107** 138301
[25] Furst E M and Squires T M 2017 *Microrheology* (Oxford: Oxford University Press)
[26] Furst E M 2005 Applications of laser tweezers in complex fluid rheology *Curr. Opin. Colloid Interface Sci.* **10** 79–86
[27] Liu Y, Edmond K V, Curran A, Bryant C, Peng B, Aarts D G A L, Sacanna S and Dullens R P A 2016 Core–shell particles for simultaneous 3d imaging and optical tweezing in dense colloidal materials *Adv. Mater.* **28** 8001–6
[28] Van Der Meer B, Weikai Q, Fokkink R G, Van Der Gucht J, Dijkstra M and Sprakel J 2014 Highly cooperative stress relaxation in two-dimensional soft colloidal crystals *Proc. Natl. Acad. Sci.* **111** 15356–61
[29] Isa L, Buttinoni I, Fernandez-Rodriguez M A and Vasudevan S A 2017 Two-dimensional assemblies of soft repulsive colloids confined at fluid interfaces *EPL (Europhys. Lett.)* **119** 26001
[30] Aveyard R, Clint J H, Nees D and Paunov V N 2000 Compression and structure of monolayers of charged latex particles at air/water and octane/water interfaces *Langmuir* **16** 1969–79
[31] Dietrich K, Renggli D, Zanini M, Volpe G, Buttinoni I and Isa L 2017 Two-dimensional nature of the active Brownian motion of catalytic microswimmers at solid and liquid interfaces *New J. Phys.* **19** 065008

[32] Juniper M P N, Besseling R, Aarts D G A L and Dullens R P A 2012 Acousto-optically generated potential energy landscapes: potential mapping using colloids under flow *Opt. Express* **20** 28707–16
[33] Juniper M P N, Straube A V, Besseling R, Aarts D G A L and Dullens R P A 2015 Microscopic dynamics of synchronization in driven colloids *Nat. Commun.* **6** 1–7
[34] Jones P H, Maragò O M and Volpe G 2015 *Optical Tweezers: Principles and Applications* (Cambridge: Cambridge University Press)
[35] Pantina J P and Furst E M 2004 Directed assembly and rupture mechanics of colloidal aggregates *Langmuir* **20** 3940–6
[36] Masschaele K, Park B J, Furst E M, Fransaer J and Vermant J 2010 Finite ion-size effects dominate the interaction between charged colloidal particles at an oil–water interface *Phys. Rev. Lett.* **105** 048303
[37] Danov K D and Kralchevsky P A 2006 Electric forces induced by a charged colloid particle attached to the water–nonpolar fluid interface *J. Colloid Interface Sci.* **298** 213–31
[38] Hurd A J 1985 The electrostatic interaction between interfacial colloidal particles *J. Phys. A: Math. Gen.* **18** L1055
[39] Park B J, Lee B and Taekyung Y 2014 Pairwise interactions of colloids in two-dimensional geometric confinement *Soft Matter* **10** 9675–80
[40] Masri D E, van Oostrum P, Smallenburg F, Vissers T, Imhof A, Dijkstra M and Alfons van B 2011 Measuring colloidal forces from particle position deviations inside an optical trap *Soft Matter* **7** 3462–6
[41] Parolini L, Law A D, Maestro A, Martin D, Buzza A and Cicuta P 2015 Interaction between colloidal particles on an oil–water interface in dilute and dense phases *J. Phys.: Condens. Matter* **27** 194119
[42] Dietrich K, Volpe G, Sulaiman M N, Renggli D, Buttinoni I and Isa L 2018 Active atoms and interstitials in two-dimensional colloidal crystals *Phys. Rev. Lett.* **120** 268004
[43] McGorty R, Fung J, Kaz D and Manoharan V N 2010 Colloidal self-assembly at an interface *Mater. Today* **13** 34–42
[44] Landau L D and Lifshits E M 1964 Theory of Elasticity Translated from the Russian by J B Sykes and W H Reid (Pergamon Press)
[45] Ramananarivo S, Ducrot E and Palacci J 2019 Activity-controlled annealing of colloidal monolayers *Nat. Commun.* **10** 1–8